Proximity-Driven Enhanced Magnetic Order at Ferromagnetic-Insulator–Magnetic-Topological-Insulator Interface

Proximity-Driven Enhanced Magnetic Order at Ferromagnetic-Insulator–Magnetic-Topological-Insulator Interface

Mingda Li,[1,2,3,*] Cui-Zu Chang,[2,†] Brian. J. Kirby,[4] Michelle E. Jamer,[5] Wenping Cui,[6] Lijun Wu,[3] Peng Wei,[2] Yimei Zhu,[3] Don Heiman,[5] Ju Li,[1,7] and Jagadeesh S. Moodera[2,8,‡]

[1]*Department of Nuclear Science and Engineering, Massachusetts Institute of Technology, Cambridge, Massachusetts 02139, USA*
[2]*Fracsis Bitter Magnet Lab, Massachusetts Institute of Technology, Cambridge, Massachusetts 02139, USA*
[3]*Condensed Matter Physics and Materials Science Department, Brookhaven National Laboratory, Upton, New York 11973, USA*
[4]*Center for Neutron Research, National Institute of Standards and Technology, Gaithersburg, Maryland 20899, USA*
[5]*Department of Physics, Northeastern University, Boston, Massachusetts 02115, USA*
[6]*Department of Physics, Boston College, Chestnut Hill, Massachusetts 02467, USA*
[7]*Department of Material Science and Engineering, Massachusetts Institute of Technology, Cambridge, Massachusetts 02139, USA*
[8]*Department of Physics, Massachusetts Institute of Technology, Cambridge, Massachusetts 02139, USA*

(Received 8 May 2015; published 17 August 2015)

Magnetic exchange driven proximity effect at a magnetic-insulator–topological-insulator (MI-TI) interface provides a rich playground for novel phenomena as well as a way to realize low energy dissipation quantum devices. Here we report a dramatic enhancement of proximity exchange coupling in the MI/magnetic-TI EuS/$Sb_{2-x}V_xTe_3$ hybrid heterostructure, where V doping is used to drive the TI (Sb_2Te_3) magnetic. We observe an artificial antiferromagneticlike structure near the MI-TI interface, which may account for the enhanced proximity coupling. The interplay between the proximity effect and doping in a hybrid heterostructure provides insights into the engineering of magnetic ordering.

DOI: 10.1103/PhysRevLett.115.087201 PACS numbers: 75.70.Cn, 61.05.fj, 75.25.-j, 75.30.Gw

The time-reversal symmetry (TRS) breaking and surface band gap opening of a topological insulator (TI) are essential ingredients necessary for towards the observation of novel quantum phases and realization for TI-based devices [1,2]. In general, there are two approaches to break the TRS: transitional-metal (TM) ion doping [3–5] and magnetic proximity effect where a magnetic insulator (MI) adlayer induces exchange coupling [3,6–8]. Doping TM impurities into a TI will introduce a perpendicular ferromagnetic (FM) anisotropy and provide a straightforward means to open up the band gap of a TI's surface state, with profound influence to its electronic structure [4,9–14]. In particular, quantum anomalous Hall effect (QAHE), where quantum Hall plateau and dissipationless chiral edge channels emerge at zero external magnetic field, has recently been realized in Cr-doped and V-doped TIs [9,10,15–20]. Ideally, compared to the doping method, proximity effect has a number of advantages, including spatially uniform magnetization, better controllability of surface state, freedom from dopant-induced scattering, as well as preserving TI intrinsic crystalline structure, etc. [21,22]. However, due to the in-plane anisotropy and low Curie temperature, such MIs are usually too weak to induce strong proximity magnetism in a TI. In fact, compared to a magnetically doped TI which can induce as large as a 50 meV surface band gap [4], the EuS-TI system has only a 7 meV gap opening due to the strongly localized Eu f orbitals [23]. Therefore, the enhancement of proximity magnetism is highly desirable to make it a valuable approach as doping hence takes full advantage.

In this Letter, we report significant enhancement of the proximity effect in MI EuS/magnetic-TI $Sb_{2-x}V_xTe_3$ hybrid heterostructure. Using polarized neutron reflectometry (PNR), we inferred an increase of proximity magnetization per unit cell (u.c.) in TI, from $1.2\mu_B$/u.c. to $2.7\mu_B$/u.c. at $x = 0.1$ doping level. High-resolution transmission electron microscopy (HRTEM) identifies the TI-EuS interfacial sharpness and excludes the false positive magnetism signal from interdiffused Eu ions into a TI. Furthermore, the proximity effect enhancement is accompanied by a decrease of the interfacial magnetization of EuS, resulting in an exotic antiferromagnetic (AFM) structure. The existence of the artificial AFM structure between FM EuS and the FM $Sb_{2-x}V_xTe_3$ is consistent with magnetometry measurements, and may shed light on creating artificial magnetic orders, such as the AFM structure reported here.

High-quality MI 6 nm EuS/15 quintuple layer (QL) magnetic TI $Sb_{2-x}V_xTe_3$ hybrid heterostructures were grown by molecular beam epitaxy under a base vacuum $\sim 5 \times 10^{-10}$ Torr, where thin films $Sb_{2-x}V_xTe_3$ were grown on clean, heat-treated sapphire (0001) substrates with V dopants coevaporated *in situ*. The EuS (111) layer was deposited *in situ* over the TI film using an electron gun. To understand the interplay between the proximity effect and TM doping, 6 nm EuS/15 QL Sb_2Te_3, 6 nm EuS /15 QL $Sb_{2-x}V_xTe_3$, and 15 QL $Sb_{2-x}V_xTe_3$ samples were fabricated. The atomic configuration of the MI–magnetic-TI heterostructure is shown in Fig. 1(a). The EuS has in-plane anisotropy [24–27] within the xz plane,

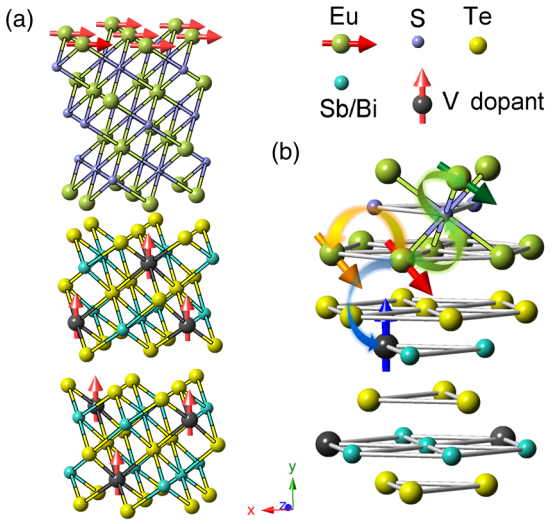

FIG. 1 (color online). (a) MI EuS–V-doped TI Sb_2Te_3 hybrid heterostructure. The arrows denote the spin direction. The V-doped TI layer has a perpendicular magnetic anisotropy, while EuS has in-plane anisotropy. Such a heterostructure may create an exotic magnetic environment near the interface, as illustrated in (b). For a given Eu ion (red arrow), it interacts with neighborhood intraplane Eu (orange arrow) through Heisenberg interaction, interplane Eu ions (green arrow) through superexchange interaction, spin-polarized states at the TI surface, and localized moments in the TI (blue arrow).

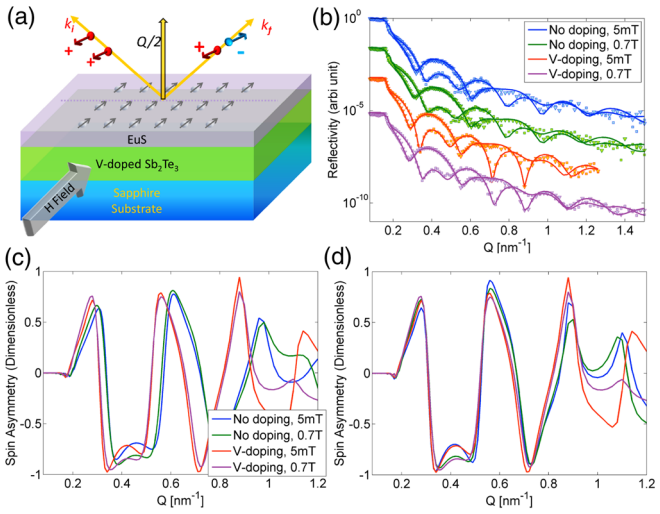

FIG. 2 (color online). (a) The configuration of PNR. k_i, k_f, and Q denote the incident, reflected, and transferred wave vectors, respectively. (b) The spin + and spin − PNR data R^+ and R^- for the $EuS/Sb_{1.9}V_{0.1}Te_3$ and EuS/Sb_2Te_3 samples, at low (5 mT) and high (0.7 T) in-plane guide fields. The fitting results are represented by solid lines and shifted for clarity. (c) The spin asymmetry for the reflectivity in (b). (d) The same spin asymmetry, but assuming control sample EuS/Sb_2Te_3 have exactly the same thickness as $EuS/Sb_{1.9}V_{0.1}Te_3$. In this way, the spin asymmetry difference is dominated by magnetic structure only. At ~0.4 nm^{-1}, the difference comes from the effect of external magnetic field, while at ~1.0 nm^{-1} the difference mainly comes from V-dopants.

while the TM-doped TI has easy axis out-of-plane [10,14,20] along the y axis. The different anisotropy directions and a strong interfacial spin-orbit coupling create a complex magnetic environment for the interfacial EuS [Fig. 1(b)]. The Heisenberg interaction, superexchange interaction [25,28], $d-f$ coupling [29] and coupling with the TI's spin texture may finally contribute to an overall augmentation of the proximity effect.

The PNR experiments were carried out using PBR beam line at the NIST CNR, from which the in-plane magnetization is extracted. The experimental setup is shown in Fig. 2(a), where the incident spin-polarized neutrons are reflected by the sample, while the spin nonflip reflectivities from both spin components (++ and −−) were collected under an external guide magnetic field. The PNR refinement is based on a multilayered substrate / TI / proximity layer /interfacial EuS / main EuS model [22]. To maximize the PNR information extraction, we did not compare the χ^2 with and without proximity effect due to limited sensitivity but presume the existence of the proximity coupling layer and optimize its magnitude.

The spin nonflip reflectivity curves for the main sample $EuS/Sb_{1.9}V_{0.1}Te_3$ and control sample EuS/Sb_2Te_3, at low (5 mT) and high (0.7 T) fields, are shown in Fig. 2(b). The refinement of PNR is performed using GenX [30]. To directly infer the possible contribution of V dopants, the corresponding spin asymmetries $SA = [(R^+ - R^-)/(R^+ + R^-)]$ are plotted [Fig. 2(c)] for the raw and thickness-adjusted data [Fig. 2(d)]. In this way, the different features of the SA in Fig. 2(d) are solely coming from the magnetic structure since the crystalline structure is adjusted identical. We see that at $Q \sim 0.4$ nm^{-1}, $\mu_0 H = 5$ mT SA for both samples with and without V dopants overlapping each other, but distinct with the $\mu_0 H = 700$ mT SA curves, indicating an effect from the guide field; while at $Q \sim 1.0$ nm^{-1}, a splitting of the SA curves for both samples at the same guide field (e.g., blue and red curves) is observed. This indicates the influence of the V dopants to magnetic structure at high Q range (spatially localized) even without fitting.

The PNR results are shown in Fig. 3. The sapphire substrate lies in the region below 0 nm. Nuclear scattering length density (NSLD, red curves) identifies the compositional contrast, where the NSLDs for each layer are correctly reproduced from PNR fitting (sapphire substrate 5.5×10^{-4} nm^{-2}, Sb_2Te_3 1.8×10^{-4} nm^{-2}, EuS 1.5×10^{-4} nm^{-2}, and amorphous Al_2O_3 capping layer 4×10^{-4} nm^{-2}), validating the fitting quality. In Fig. 3(a), without the EuS proximity layer, the V dopants in the $Sb_{1.9}V_{0.1}Te_3$ sample contribute to only $0.2\mu_B$/u.c. in-plane magnetization at $\mu_0 H = 0.7$ T, indicating a very strong perpendicular FM anisotropy. This is consistent with the result in the inset of Fig. 4(a), and facilitates us in obtaining reliable PNR refinement by fixing the magnetization of the

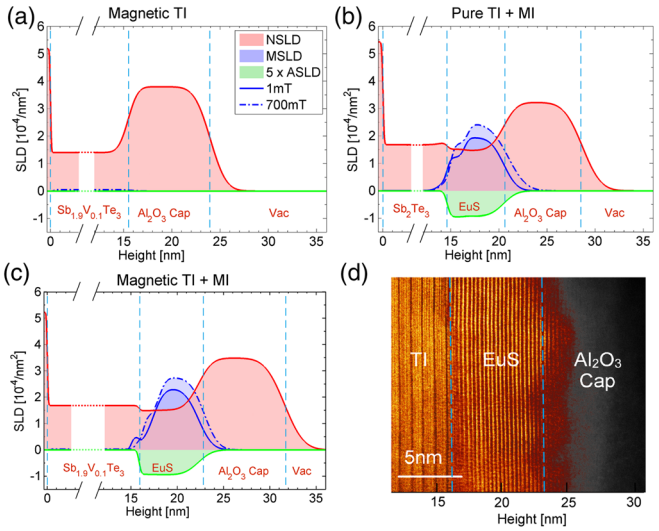

FIG. 3 (color online). PNR fitting profiles of doping-only sample $Sb_{1.9}V_{0.1}Te_3$ (a), proximity-only sample EuS/Sb_2Te_3 (b), and hybrid heterostructure $EuS/Sb_{1.9}V_{0.1}Te_3$ (c). NSLD, MSLD, and ASLD denote the nuclear, magnetic, and absorption scattering length density, which are measures of chemical contrast, magnetization, and neutron absorption, respectively. The proximity effect is identified directly as the finite magnetization signal (blue curves) in the region of a TI near the TI-EuS interface (~15 nm). The absorption-free feature in this region excludes the possible contribution which solely comes from interdiffused Eu ions. We see clearly that with V doping, the proximity magnetism is enhanced as a bump in (c), accompanied with a further suppression of magnetism of interfacial EuS (15–18 nm). (d) HAADF TEM image of the $EuS/Sb_{1.9}V_{0.1}Te_3$ hybrid heterostructure. A sharp interface between the TI-MI is developed, indicating an epitaxial growth of EuS. This independent TEM result is quite consistent with (c) for uniformly distributed ASLD of EuS. The islandlike crystalline facets between the EuS and Al_2O_3 cap is also in very good agreement with the roughness in (c).

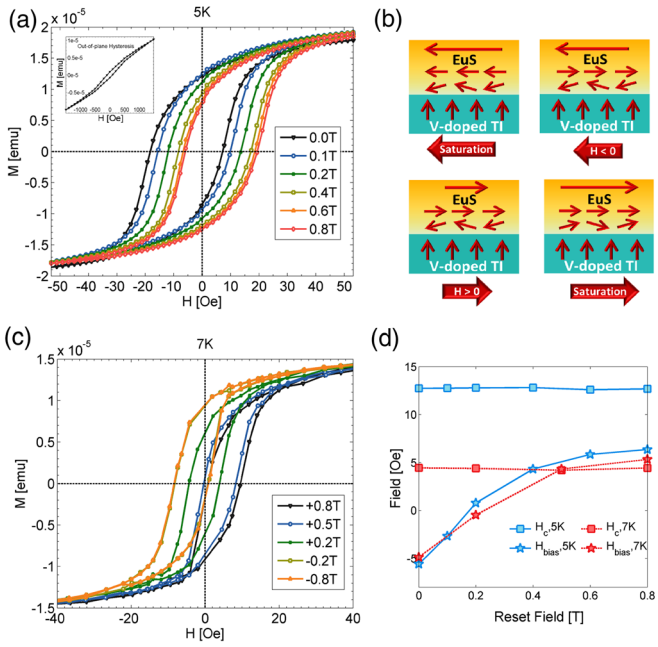

FIG. 4 (color online). Magnetic measurements of a 2 nm EuS/10QL $Bi_1.9V_0.1Te_3$ hybrid heterostructure using a SQUID magnetometer. (a),(c) In-plane hysteresis at 5 K(a) and 7 K(c), respectively, showing a negative EB following a set field of −1 T which can be switched to positive bias by applying a positive resetting field. Inset of (a) is the out-of-plane magnetic hysteresis of the same sample, showing a finite remanent moment. (b) Schematic interfacial magnetic structure, where the interfacial EuS moments (horizontal arrows, the long arrow on the top of EuS means a saturated magnetization) are pinned by the exchange-coupled moments in the presence of a V-doped TI (vertical arrows). (d) EB and coercive field as a function of the in-plane resetting field at 5 K and 7 K, respectively.

magnetic TI layer. The magnetic SLD (MSLD, blue curves) at $\mu_0 H = 5$ mT and 700 mT guide fields at $T = 5$ K are also plotted. In Fig. 3(b), for the EuS-pure TI sample, we see a penetration of magnetization into the TI, which is a direct signature of proximity magnetism. Unlike the EuS region where strong absorption SLD (ASLD) is always accompanied due to the Eu ions' extremely large neutron absorption cross section, the penetrated magnetization into the TI does not show any absorption (~14–15 nm), indicating that such magnetism in a TI is not from ferromagnetic Eu ions interdiffusing into Sb_2Te_3, but from the proximity effect. The absence of interdiffusion is also consistent with our TEM result in Fig. 3(d), where a sharp interface between epitaxially grown EuS and $Sb_{1.9}V_{0.1}Te_3$ is developed.

The magnetization at the interface in proximity structures is greatly enhanced when V dopants exist, from $1.2\mu_B$/u.c. [Fig. 3(b), without V doping] to $2.7\mu_B$/u.c. [Fig. 3(c), V doped]. In both cases, the penetration depth of proximity is ~1 nm, consistent with the Bi_2Se_3/EuS interface [22]. Besides, the in-plane magnetization of EuS drops dramatically near the interface, from $\sim 3\mu_B$/u.c. without V dopants to $\sim 0.5\mu_B$/u.c. with V doping, at $\mu_0 H = 5$ mT. This is due purely to the magnetic effect instead of interfacial roughness since the ASLD is flat near the TI interface. On the contrary, the magnetization drop at the EuS/Al_2O_3 interface (~23 nm) is due to the Stranski–Krastanov growth [31], leading to a thickness variation and formation of an island. This is directly confirmed from the Z-contrast high-angle angular-dark-field (HAADF) HRTEM image [Fig. 3(d)]. At higher field $\mu_0 H = 0.7$ T, an increase of the in-plane EuS magnetism is accompanied with a drop of proximity effect into the TI. Since only the perpendicular direction magnetism will contribute to the proximity effect [1], a high in-plane guide field tends to align the EuS moment in plane and reduce the proximity.

To understand the origin of the drop of interfacial magnetism of EuS, we examined the exchange bias (EB) of the magnetic hysteresis measurements. Figure 4 plots the

results of low-field in-plane hysteresis measurements of a 2 nm EuS/10QL $Bi_1.9V_0.1Te_3$ hybrid heterostructure instead of Sb_2Te_3 since both belong to the Bi_2Se_3 TI family and share very similar crystalline structure; Sb_2Te_3 is more suitable for PNR studies due to less interstitial V defects, Bi_2Te_3 is better for SQUID magnetometry due to higher diamagnetic susceptibility. Figures 4(a) and 4(c) show that the EB can be switched from negative to positive by a field $\mu_0 H = \pm 1$ T, at 5 K and 7 K, respectively, where the corresponding EB and coercivity are plotted in Fig. 4(d). We adopt the traditional approach for EB measurement [32–34] at various resetting fields, where the EB was initially set negative by applying a field of −1 T, followed by a positive field then measuring the low-field hysteresis [35]. This was repeated for resetting fields from 0 to +0.8 T, where the bias is shifted from $H_{\text{bias}} = -5$ to +6 Oe. Results of the exchange biasing strongly suggests the existence of an AFM structure or possible magnetic frustration [36], and is quite striking since our system is only composed of two strong FMs. The possible magnetic configuration is illustrated in Fig. 4(b), where a V-doped TI keeps a perpendicular anisotropy, while interfacial AFM structure is created to cause the EB.

To further understand the implication of the results in Fig. 4, we develop a phenomenological energy model to describe the FM-AFM coupling. The anisotropic energy for bulk EuS can be written as [26]

$$E_{\text{an}} = \kappa_1 M_s t(\alpha_1^2\alpha_2^2 + \alpha_1^2\alpha_3^2 + \alpha_3^2\alpha_2^2) + \kappa_2 M_s t\alpha_1^2\alpha_2^2\alpha_3^2 \quad (1)$$

where α_i is the directional cosine along the ith direction, M_s is the saturation magnetism per area, t is the thickness of the FM layer, and the anisotropic constants $\kappa_1 = -19.6$ Oe and $\kappa_2 = -4.6$ Oe at $T = 1.3$ K [26]. Since our interest is in thin film structures with a single symmetry axis [y axis in Fig. 1(a)], Eq. (1) could be rewritten using a simplified model for hexagonal and cubic lattice [37],

$$E_{\text{an}} = K_1 M_s t\sin^2(\theta) + K_2 M_s t\sin^4(\theta) \quad (2)$$

where $K_1 = \kappa_1 = -19.6$ Oe, $K_2 = -\frac{7}{8}\kappa_1 + \frac{1}{8}\kappa_2 = 16.6$ Oe, θ is the angle between the magnetization and the symmetry axis. Since $K_1 < 0$, $\theta = \pi/2$ corresponds in the present case for EuS showing easy-plane anisotropy within the xz plane. For a thin film, we further define $K_{1,\text{eff}} = K_s/t + K_1$. We require the surface anisotropy constant $K_s > 0$, since for the thinner sample $K_{1,\text{eff}}$ will be closer to zero, indicating a rotation of easy-plane to out-of-plane direction, resulting in a magnetic canting which is reasonable for compensated thin film interfaces [33].

Taking into account the external magnetic field H and the FM-AFM coupling J, the total energy could be written as

$$E = -HM_s t\sin(\theta) - J\sin(\theta) + \left(K_1 + \frac{K_s}{t}\right) M_s t\sin^2(\theta) + K_2 M_s t\sin^4(\theta). \quad (3)$$

At saturation field configuration $\theta = \pm\pi/2$ and considering the energy extreme, we obtain the bias field and coercivity

$$H_{\text{bias}} = -\frac{J}{Mt}, \qquad H_c = 2K_1 + 4K_2 + \frac{2K_s}{t}, \quad (4)$$

respectively.

The anisotropic coefficients strongly depend on temperature [37]. In the mean-field approximation, the temperature dependence of the anisotropy can be expressed using the Callen and Callen theory as [38]

$$K(T) = K(0)\left(1 - \frac{T}{T_c}\right)^{[n(n+1)/4]} \quad (5)$$

where n is the order of anisotropy constant, $n(K_1) = 2$, and $n(K_2) = 4$. Assuming that the Curie temperature of EuS is $T_c = 17$ K, we obtain the temperature dependence of anisotropy constants as shown in Table I. One remarkable feature for this model is that the surface anisotropy K_s/t calculated from experimental values and Eq. (4) is consistent with Eq. (5), giving 7.2 Oe vs 7.1 Oe at 7 K. Finally, this yields a surface anisotropy $K_s = 0.0014$ erg cm^{-2} by assuming a 2.5×10^{-5} emu saturation and 5 mm^2 sample area. This term is the origin of magnetic canting of interfacial EuS.

Contrary to the strong T dependence of anisotropy, the bias field H_{bias} thus AFM-FM coupling constant J has a weak dependence with temperature, indicating an origin of FM-AFM coupling different from magnetic crystalline anisotropy such as the prominent role of spin-orbit interaction and spin-momentum locking at the TI surface.

To summarize, we have reported a large enhancement of proximity exchange coupling strength in a MI–magnetic-TI hybrid heterostructure. This overcomes the major disadvantage in MI-TI heterostructures where the proximity effect is considered weak [23]. To our knowledge, this is also the first report uniting TM doping and proximity effect

TABLE I. Temperature dependence of the anisotropy constants.

$T_c = 17$ K	1.3 K	5 K	7 K
K_1(Oe)	−19.6[a]	−13.10[b]	−9.96[b]
K_2(Oe)	+16.6[a]	7.41[b]	4.29[b]
H_c(Oe)	⋯	12.7[c]	4.4[c]
K_s/t(Oe)	13.8[b]	9.3[d]	7.2[d]; 7.1[b]

[a]Reference [26].
[b]Equation (5).
[c]Measurements in Fig. 4.
[d]Equation (4).

in a MI. Here, the magnetic TI with strong perpendicular anisotropy compensates the weakness of the MI with in-plane anisotropy. Since the energy gap of the magnetic TI at Γ point satisfies $E_g \propto M$ [39], when treated as mean-field virtual crystal approximation, we have $M \propto x \propto T_C$ valid [40], where x is dopant concentration. In this regard, the interfacial magnetization enhancement implies an increased energy gap hence an increased working temperature of the interfacial magnetic order. The reduction of interfacial magnetism is consistent with the EB result, where an AFM structure is artificially created, where a $K_s = 0.0014\ \mathrm{erg\,cm^{-2}}$ surface anisotropy is extracted. Despite this value being small compared to the stronger examples such as the Au-Co interface [41], this approach provides fruitful avenue to tailor new magnetic structure at TI-MI interfaces.

M. L. and C. Z. C. would thank the helpful discussion with Prof. Albert Fert. J. S. M. and C. Z. C. are thankful for support from the STC CIQM under NSF Grant No. DMR-1231319, NSF DMR Grant No. 1207469 and ONR Grant No. N00014-13-1-0301, and MRSEC Program of the NSF under Award No. DMR-0819762. M. J. and D. H. acknowledge support from NSF DMR-907007 and NSF ECCS-1402738. L. W. and Y. Z. were supported by DOE-BES under Contract No. DE-SC0012704. M. L. and J. L. acknowledge support from NSF DMR-1410636.

*mingda@mit.edu
†czchang@mit.edu
‡moodera@mit.edu

[1] X.-L. Qi and S.-C. Zhang, Rev. Mod. Phys. **83**, 1057 (2011).
[2] M. Z. Hasan and C. L. Kane, Rev. Mod. Phys. **82**, 3045 (2010).
[3] P. Wei, F. Katmis, B. A. Assaf, H. Steinberg, P. Jarillo-Herrero, D. Heiman, and J. S. Moodera, Phys. Rev. Lett. **110**, 186807 (2013).
[4] Y. Chen *et al.*, Science **329**, 659 (2010).
[5] M. Li, C.-Z. Chang, L. Wu, J. Tao, W. Zhao, M. H. W. Chan, J. S. Moodera, J. Li, and Y. Zhu, Phys. Rev. Lett. **114**, 146802 (2015).
[6] M. Lang *et al.*, Nano Lett. **14**, 3459 (2014).
[7] I. Vobornik, U. Manju, J. Fujii, F. Borgatti, P. Torelli, D. Krizmancic, Y. S. Hor, R J. Cava, and G. Panaccione, Nano Lett. **11**, 4079 (2011).
[8] A. Kandala, A. Richardella, D. W. Rench, D. M. Zhang, T. C. Flanagan, and N. Samarth, Appl. Phys. Lett. **103**, 202409 (2013).
[9] C.-Z. Chang, W. Zhao, D. Y. Kim, H. Zhang, B. A. Assaf, D. Heiman, S.-C. Zhang, C. Liu, M. H. W. Chan, and J. S. Moodera, Nat. Mater. **14**, 473 (2015).
[10] C.-Z. Chang *et al.*, Science **340**, 167 (2013).
[11] S.-Y. Xu *et al.*, Nat. Phys. **8**, 616 (2012).
[12] Y. Hor *et al.*, Phys. Rev. B **81**, 195203 (2010).
[13] C.-Z. Chang *et al.*, Phys. Rev. Lett. **112**, 056801 (2014).
[14] C.-Z. Chang, Adv. Mater. **25**, 1065 (2013).
[15] X.-L. Qi, T. L. Hughes, and S.-C. Zhang, Phys. Rev. B **78**, 195424 (2008).
[16] R. Yu, W. Zhang, H.-J. Zhang, S.-C. Zhang, X. Dai, and Z. Fang, Science **329**, 61 (2010).
[17] C.-X. Liu, X.-L. Qi, X. Dai, Z. Fang, and S.-C. Zhang, Phys. Rev. Lett. **101**, 146802 (2008).
[18] X. Kou, Phys. Rev. Lett. **113**, 137201 (2014).
[19] J. Checkelsky, R. Yoshimi, A. Tsukazaki, K. S. Takahashi, Y. Kozuka, J. Falson, M. Kawasaki, and Y. Tokura, Nat. Phys. **10**, 731 (2014).
[20] C.-Z. Chang, P. Wei, and J. S. Moodera, MRS Bull. **39**, 867 (2014).
[21] M. Li, W. Cui, J. Yu, Z. Dai, Z. Wang, F. Katmis, W. Guo, and J. Moodera, Phys. Rev. B **91**, 014427 (2015).
[22] V. Lauter, F. Katmis, B. Assaf, and J. Moodera, in APS March Meeting Abstracts, Vol. W (2014), p. 42.00007, Http://meetings.aps.org/Meeting/MAR14/Event/215903.
[23] S. Eremeev, Phys. Rev. B **88**, 144430 (2013).
[24] J. Kuneš and W. E. Pickett, Physica (Amsterdam) **359B–361B**, 205 (2005).
[25] L. Liu, Solid State Commun. **46**, 83 (1983).
[26] M. Franzblau, G. E. Everett, and A. Lawson, Phys. Rev. **164**, 716 (1967).
[27] S. Von Molnar and A. Lawson, Phys. Rev. **139**, A1598 (1965).
[28] W. Boncher, H. Dalafu, N. Rosa, and S. Stoll, Coord. Chem. Rev. **289–290**, 279 (2015).
[29] V.-C. Lee and L. Liu, Solid State Commun. **48**, 795 (1983).
[30] M. Björck and G. Andersson, J. Appl. Crystallogr. **40**, 1174 (2007).
[31] A. Pimpinelli and J. Villain, *Physics of Crystal Growth* (Cambridge University Press, Cambridge, England, 1998), Cambridge Books Online.
[32] M. Kiwi, J. Magn. Magn. Mater. **234**, 584 (2001).
[33] R. Stamps, J. Phys. D **33**, R247 (2000).
[34] J. Nogués and I. K. Schuller, J. Magn. Magn. Mater. **192**, 203 (1999).
[35] R. Wen-Bin, M.-C. He, B. You, Z. Shi, S.-. Zhou, M.-W. Xiao, Y. Gao, W. Zhang, L. Sun, and J. Du, Chin. Phys. B **23**, 107502 (2014).
[36] C. Schlenker, S. Parkin, J. Scott, and K. Howard, J. Magn. Magn. Mater. **54–57**, 801 (1986).
[37] R. Skomski, *Simple Models of Magnetism* (Oxford University Press, Oxford, 2008).
[38] R. Skomski, O. N. Mryasov, J. Zhou, and D. J. Sellmyer, J. Appl. Phys. **99**, 08E916 (2006).
[39] W. Luo and X.-L. Qi, Phys. Rev. B **87**, 085431 (2013).
[40] W. Qin and Z. Zhang, Phys. Rev. Lett. **113**, 266806 (2014).
[41] P. Bruno, J. Phys. F **18**, 1291 (1988).